Supplementary information for:

A Weakly Ion Pairing Electrolyte Designed for High Voltage Magnesium Batteries

Chang Li,[a, b] Rishabh Guha,[b] Abhinandan Shyamsunder,[a, b] Kristin Persson[b,c,d*] and Linda F. Nazar [a, b*]

[a] Department of Chemistry and the Waterloo Institute for Nanotechnology, University of Waterloo, Ontario N2L 3G1, Canada

[b] Joint Center for Energy Storage Research, Argonne National Laboratory, Lemont, Illinois 60439, United States

[c] Molecular Foundry, Lawrence Berkeley National Laboratory, 1 Cyclotron Road, Berkeley, California 94720, United States

[d] Department of Materials Science and Engineering, UC Berkeley, Berkeley, California 94720, United States

Experimental methods

Preparation of electrolytes

Mg(TFSI)$_2$ (Solvionic, 99.5%) was dried in a Buchi vacuum oven at 150 °C for over three days. DME (Sigma-Aldrich, 99.5%), G2 (Sigma-Aldrich, 99.5%), DEE (Sigma-Aldrich, 99.5%), BTFE (Synquest Labs), TMP (Sigma-Aldrich, ≥99%), TEP (Sigma-Aldrich, ≥99.8%), TPP (Sigma-Aldrich, 99%), TBP (Sigma-Aldrich, ≥99%) and TAP (Fisher scientific, 98%) were dried by molecular sieves (Sigma-Aldrich, 3Å) for over 24 hours before use. All salts, solvents and additives were stored in an Ar-filled glove box with H$_2$O and O$_2$ levels less than 0.1 ppm. As shown in **Table S1**, a specific mass of Mg(TFSI)$_2$ was mixed with various solvents at specific volume ratios and stirred at 25 °C for 2 min to fully dissolve the salt. Phosphate additives were added to the above solution and continuously stirred for half an hour to obtain the electrolytes.

Electrochemical measurements

Coin cells (2032) were used in this study. Mg foils (thickness: 100 μm, Changsha Rich Nonferrous Metals Co., Ltd) were polished by sandpaper before being punched into small disks (diameter: ~12.7 mm, mass: ~22 mg) for cell assembly, and glass fiber separators were used (diameter: 16 mm) with 100 μL electrolyte in each cell. A VMP3 potentiostat/galvanostat station (Bio-Logic) was employed for linear sweep voltammetry (LSV) studies at a sweep rate of 5 mV s^{-1}, using three-electrode Perfluoralkoxy (PFA)-based Swagelok-type cells with Mg as the reference electrode, and Al foil (diameter: 11 mm) as both working and counter electrodes.

To accurately measure the coulombic efficiency, Mg‖Au asymmetric cells were assembled and tested based on a previously reported protocol.[1] Specifically, the Au substrates (diameter: 11 mm) were preconditioned for 10 cycles at a current density of 0.5 mA cm^{-2} with plating for 15 min and stripping at a cut-off voltage of 1.5 V. Another 15 min Mg plating cycle was used to establish a reservoir (Q$_r$), followed by 3 min stripping/plating (Q$_c$) for 10 cycles (*n*), and a final complete strip (Q$_s$) at 1.5 V. The average CE can be calculated as $(nQ_c + Q_s)/(nQ_c + Q_r)$.

For polyaniline (PANI)‖Mg or pyrene-4,5,9,10-tetraone (PTO)‖Mg full cells, PANI (Fisher Scientific, emeraldine base) or PTO (Chemscene) was first ball milled with Ketjen black™ carbon at a weight ratio of 4:5 for 100 min at 250 rpm. Then, the PANI electrode was fabricated by mixing the above mixture with polytetrafluoroethylene (Sigma-Aldrich, 60 wt% dispersion in H$_2$O) at a weight ratio of 9:1 using isopropanol as the dispersion agent. Due to the poor electronic conductivity, the relatively high carbon content is used to fabricate electrodes based on previous

studies.[2] The obtained free-standing PANI cathode was dried at 60 °C overnight and punched into small disks (diameter: 8 mm) with an active material loading of around 2.5 mg cm^{-2}. The cathode was pressed on Ti mesh (diameter: 11mm) before being tested in full cells under different C-rates at 25 °C.

Impedance analysis. The charge transfer resistance of two-electrode Mg||Mg symmetric coin cells in different electrolytes was measured by electrochemical impedance spectroscopy (EIS) with a voltage amplitude of 10 mV in the frequency range of 1 MHz to 100 mHz. The cell was cycled for 10 cycles at 0.1 mA cm^{-2} (0.1 mAh cm^{-2}) and rested for 10 min to reach equilibrium before the EIS measurement. All equivalent circuit fits were performed using the RelaxIS software package V3.

Materials characterisation

Raman spectra were collected using a 532 nm laser (Raman HORIBA HR800). Spectra were obtained using 3-5 accumulations with a total acquisition time ranging from 10-20 minutes under a 10x objective lens. NMR measurements were carried out on a Bruker Advance 300 MHz instrument. ^{1}H, ^{13}C and ^{31}P NMR experiments were carried at 300, 75 and 121 MHz, respectively. ^{1}H and ^{13}C NMR peaks reported are relative to the residual solvent (CDCl$_3$) peak at 7.26 ppm (^{1}H) and 77.0 ppm (^{13}C). ^{31}P NMR spectra are reported relative to the peak of 85% H$_3$PO$_4$ (0 ppm). NMR tubes equipped with a coaxial insert filled with CDCl$_3$ were used in the measurements, to avoid contamination of solvent with electrolyte solutions. VT NMR measurements were also carried out on the same instrument equipped with a BCU II unit. Shimming was performed for all temperatures studied to ensure accurate chemical shift values. HSQC experiments were carried out to correlate the chemical shift of protons (F2 axis) to the ^{13}C chemical shift (F1 axis) of their directly attached carbons. To characterize cycled Mg anodes, all electrodes disassembled from the cells were washed three times with DME, dried at room temperature *in vacuo* overnight and stored in an Ar-filled glove box before each study. The electrodes were directly transferred into the SEM, XPS or TEM instruments with exposure for less than 10 seconds. The scanning electron microscopy (SEM) images of Mg plating/stripping morphologies and energy-dispersive X-ray spectra (EDX) were collected on a Zeiss Ultra field emission SEM instrument. XPS experiments were conducted on a Thermo Scientific K-Alpha XPS instrument. CasaXPS software was used to conduct XPS data analysis, where the C *1s* peak of 284.8 eV was used to calibrate the binding

energies. Spectral fitting was based on Gaussian-Lorentzian functions and a Shirley-type background.

TEM sample preparation was performed by the Canadian Centre for Electron Microscopy using a Zeiss Crossbeam 350 FIB-SEM. Due to the suspected sensitivity of the surface material to both the ion and electron beams, the samples were coated with a relatively thick plasma-sputtered chromium coating prior to the FIB-SEM work. This coating protected the surface during the electron beam-induced deposition and subsequent ion beam-induced deposition of the tungsten protection layer. The TEM samples were extracted from the particles by conventional FIB methods. The thinning necessary for electron transmission was performed under cryogenic conditions at approximately -135°C. The final ion beam probe of the 30 kV thinning was 40 pA. This was followed by a ~7° glancing-angle low voltage cleaning step applied to both sides with a 2 kV 50 pA ion beam. The resulting TEM sample was loaded into a Spectra Ultra 30-300kV TEM (Thermo Fisher Scientific) equipped with a Cs probe and image aberration correctors that was operated at 200 kV. An attached Ultra-X EDS detector was used to map Mg interface and collect EELS data. The EDS Maps were post-processed using Velox Software.

Molecular dynamics simulations

Classical MD simulation trajectories of the multivalent bulk electrolyte systems were used to analyze the local environment around the Mg^{2+} ions and extract the populations of the different solvated clusters. The density, molecular weights and concentration fractions of the electrolyte constituents was used to determine the appropriate molecules for each species in the three systems. Packmol[3] was used to generate the initial configurations of the simulation cells. The particle-particle particle-mesh method[4] was used to handle the long-range interactions and cut-off distances were set at 10 and 12 Å for the Lennard-Jones (LJ) and Coulombic interactions respectively. A box length of more than twice the cut-off distances was ensured as the dimensions of the energy minimized systems were at least 55 Å per side. For every system, the reported statistics were averaged over three replicate simulation cells with different initial configurations. The equilibration procedure comprised of a 2 ns NPT ensemble run at an elevated temperature of 600 K and 1 bar, followed by 2 ns of cooling to 298 K and a final NPT equilibration of 1 ns at 298 K. Following the equilibration, the data was sampled from a 10 ns NVT ensemble run performed at 298 K. The open-source code, LAMMPS[5] was used to perform all the MD simulations.

The Generalized Amber Force Field (GAFF)[6] was used to generate the bond, angle, and dihedral parameters for neutral DME, TEP, G2 and BTFE molecules as well as the TFSI⁻ anion. For the neutral molecules, the LJ GAFF parameters were obtained from the moltemplate utility, and the antechamber program was used in conjunction with the AM1-BCC[7] charge scaling protocol to assign the partial charges on each atom. The LJ parameters and partial charges for the TFSI⁻ anion was adopted from a previous study.**Error! Bookmark not defined.** These TFSI⁻ parameters have been previously successful in reproducing experimental X-ray pair distribution functions (PDFs). Mg^{2+} LJ parameters designed to accurately capture the ion-oxygen coordination[8] in aqueous systems were adapted for this work as oxygen was the primary Mg^{2+}-coordinating species in all the electrolyte systems. The partial charges on the TFSI⁻ anion and the Mg^{2+} cations were subsequently scaled by a factor of 0.8 to account for the electronic polarization in these non-polarizable force-fields[9] and ameliorate potential artefacts like ion-pairing overestimation and increased binding.[10,11]

The population analysis of the different solvation shells was performed using the SolvationAnalysis[12] python plugin developed over MDAnalysis[13]. As a first step, the cut-off distance for the species comprising the first solvation shell was obtained from the radial distribution functions (**Fig. S12**) of the different molecules coordinating with Mg^{2+} (DME, G2, TEP and TFSI⁻). Subsequently, the frequency of the different solvation configurations was calculated. The percentage population of the most abundant configurations is compiled in **Fig. S13**. The Mg^{2+}-coordination of each molecule was calculated by averaging over all the solvation shell configurations in the trajectory. The free Mg^{2+} fraction corresponds to the solvation shells with no TFSI⁻.

Density Functional Theory calculations

The free energy calculations for the contact ion pair C-S bond dissociation was performed by combining automated workflows and Q-Chem 5.4[14]. The frequency-flattening optimization (FFOpt)[15] workflow implemented in atomate[16] was used to simultaneously optimize the structure to a true minimum and obtain thermochemical quantities from the vibrational frequencies. The workflow iteratively performs successive geometry optimizations and frequency calculations until there are either none or a single negligible negative frequency (<15 cm⁻¹). This approach ensures that the optimized structure is a true minimum and not an nth order saddle point. Moreover, it also provides the enthalpy and entropy, necessary for the free energy calculations. Initial structures

were optimized with the range-separated GGA hybrid functional, ωB97X-D[17] which employs an empirical atomic-pairwise dispersion correction for improving the non-covalent interactions. The def2-SVPD[18] basis set was used with a PCM dielectric[19] to account for solvation effects. The electronic energies of the optimized structures were refined with a single point calculation using the ωB97M-V meta GGA range separated hybrid[20] and a larger def2-TZVPPD basis set[21]. The dielectric constant for the DME: TEP and the CEPE system was determined by a fractional sum of dielectric constants of participating electrolyte species in the system (**Table S4**). The dissociated TFSI radical was optimized at different spin multiplicities and the optimized singlet was found to be the lowest energy product for the bond dissociation reaction (**Fig. S6**).

Evaluations of the binding energy involved geometry optimizations of complete solvation shells. The use of the range separated GGA (ωB97X-D) for these calculations became computationally expensive, especially for the larger clusters. Therefore, we resorted to using the dispersion corrected GGA, B97-D3[22] functional with a def2-SVPD basis set for the geometry optimization, followed by the same single point correction scheme (ωB97M-V with def2-TZVPPD) as the BDE calculations. The first two solvation shells dominated the population fraction (90.4%) in the Mg(TFSI)₂/DME system, and the binding energy calculations were limited to these two possible configurations for this system. In case of the Mg(TFSI)₂/DME: TEP and the Mg(TFSI)₂/CEPE system, the binding energy was calculated for the five solvation shells with the highest average population fraction.
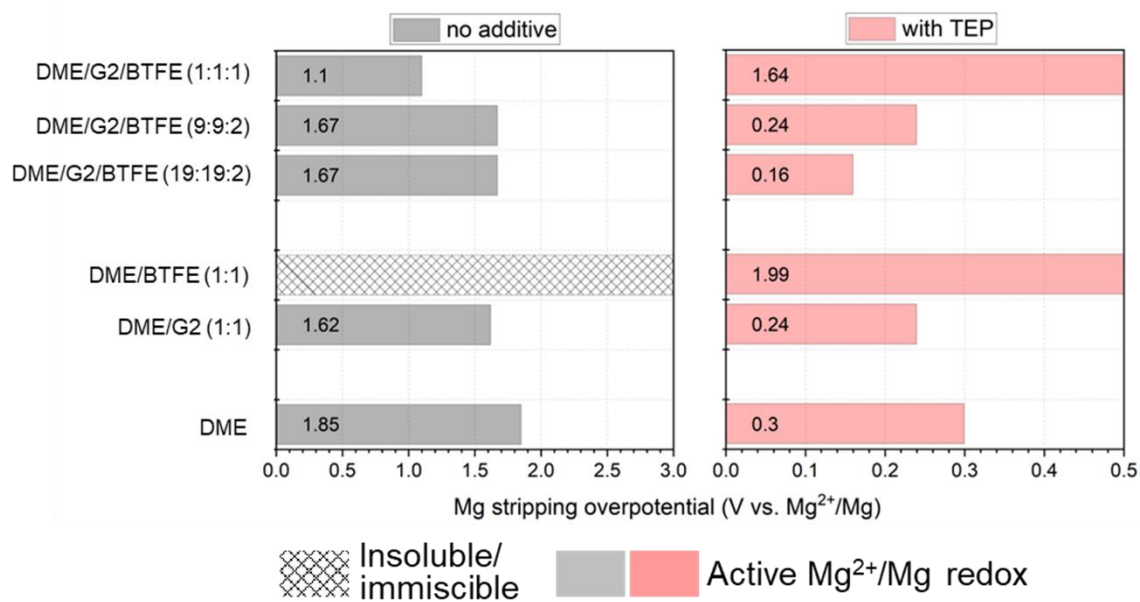
Fig. S1 The summary of Mg stripping overpotential of different electrolytes in Mg symmetric cells. The current density is 0.1 mA cm^{-2} with an areal capacity of 0.1 mAh cm^{-2} in all measurements. The sparse pattern and colors of each column represent the solubility/miscibility of electrolytes and the activity of Mg^{2+}/Mg redox, respectively. The value of Mg stripping overpotential of electrolytes with active Mg^{2+}/Mg redox is shown by the length of column and labeled by the corresponding numbers. The concentration of TEP is 10 vol% of all other solvents.
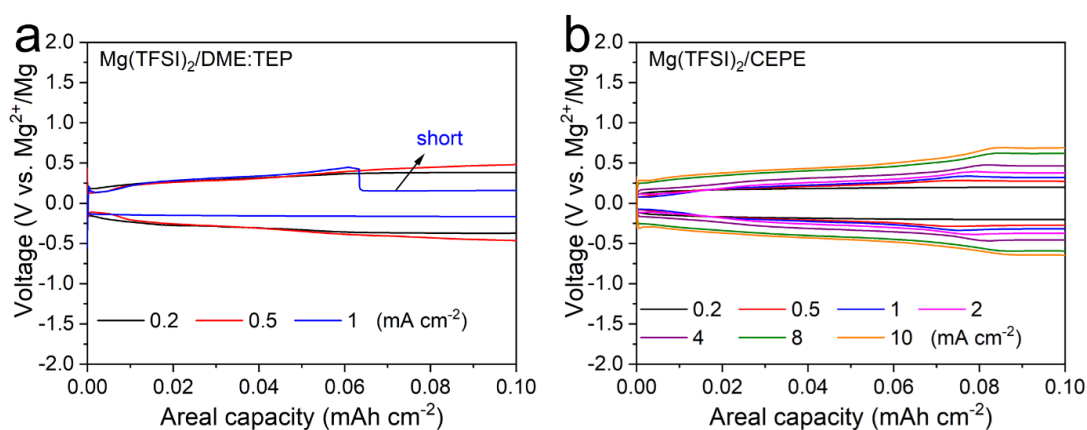
Fig. S2 Selected voltage profiles of TEP-based electrolytes at different current densities in Mg symmetric cells: (a) Mg(TFSI)$_2$/DME:TEP; (b) Mg(TFSI)$_2$/CEPE. In CEPE, the plating and stripping curves show distinct two plateaus, which can be ascribed to the initial Mg nucleation and subsequent growth process on pre-deposited nuclei.
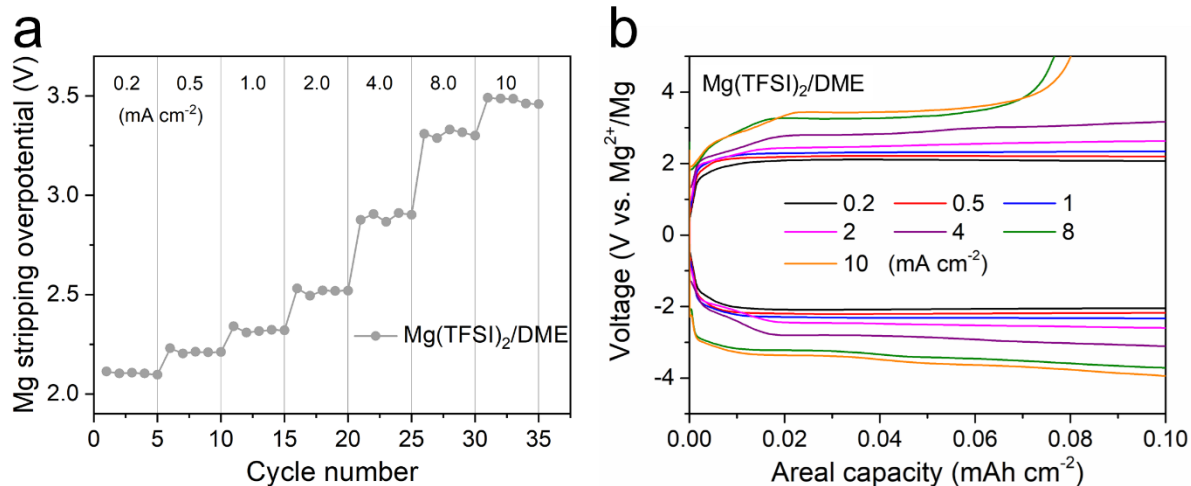
Fig. S3 Rate performance of Mg(TFSI)$_2$/DME in Mg symmetric cells. (a) Mg stripping overpotentials at different current densities; (b) selected voltage profiles at 0.2-10 mA cm^{-2} with a fixed areal capacity of 0.1 mAh cm^{-2}.
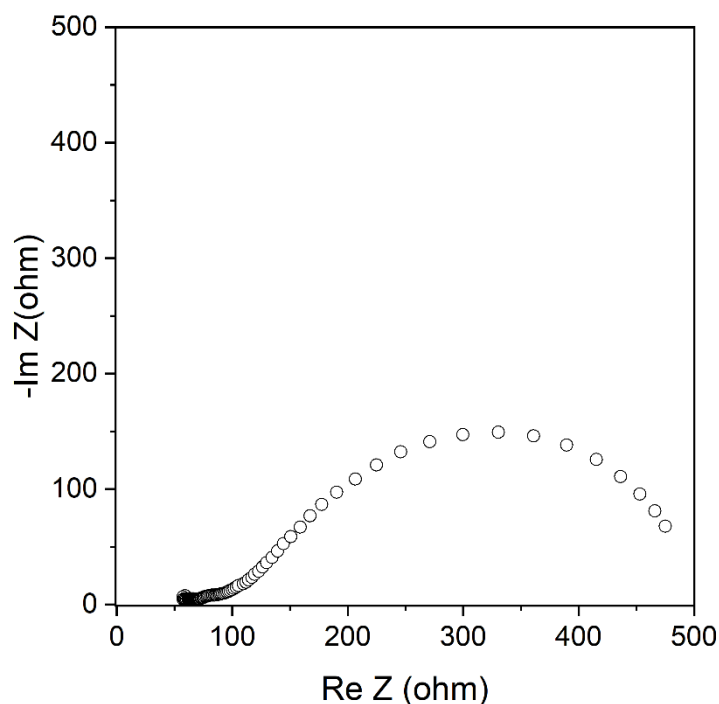
Fig. S4 Nyquist plot of a Mg||Mg symmetric cell in Mg(TFSI)$_2$/CEPE after 7000 hours at 2 mA cm^{-2} and 2 mAh cm^{-2}. The measurement was conducted immediately after cycling to prevent overlooking any soft short, since resting the cell may cause a soft short to become invisible as demonstrated in previous work by Zhi *et al.* (Q. Li, A. Chen, D. Wang, Z. Pei and C. Zhi. *Joule*, 2022, **6**, 1-7). The exhibited charge transfer resistance of around 400 Ω confirms the absence of any (soft) short. In addition, we note this value is significantly higher than that of the initial cycles (**Fig. 1f**), which can be ascribed to the formation of an SEI on the Mg surface during initial plating/stripping. The presence of this SEI can prevent continuous electrolyte decomposition, as confirmed by the stabilized overpotential (~500 mV) for plating/stripping over 7000 hours.
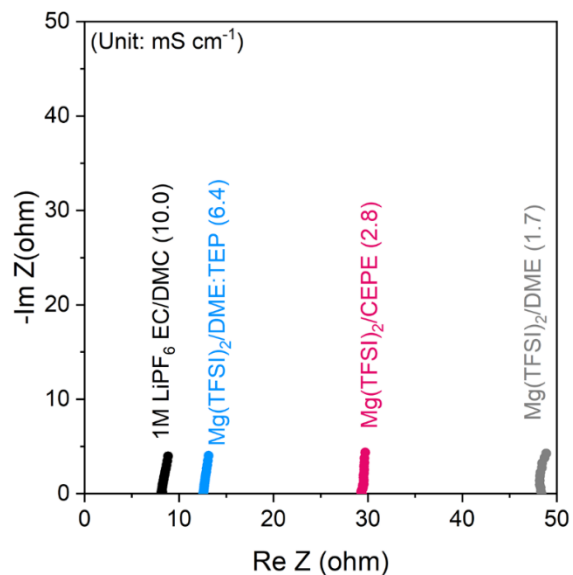
Fig. S5 The ionic conductivity of different electrolytes measured in Pt||Pt symmetric cells using 1 M LiPF$_6$ in EC/DMC (10 mS cm^{-1}) as the reference electrolyte.
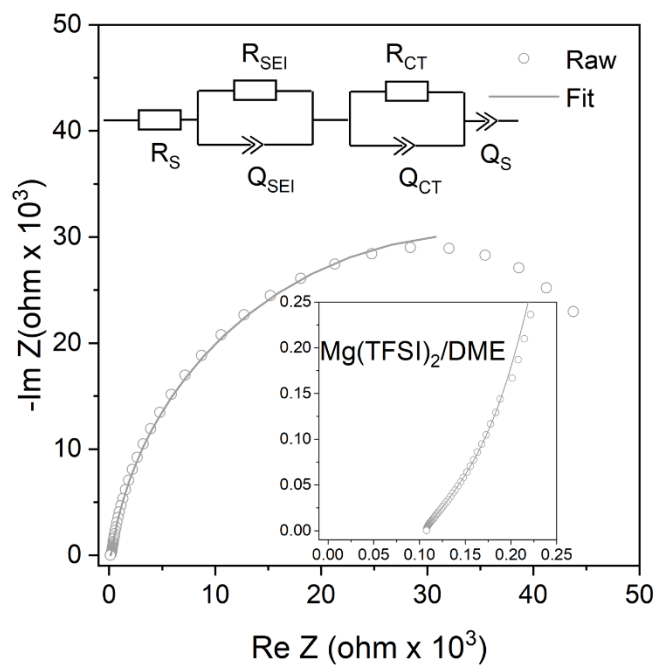
Fig. S6 Nyquist plots of a Mg||Mg symmetric cell after 10 cycles in Mg(TFSI)$_2$/DME. The data were fit (solid line) with the indicated equivalent circuit.
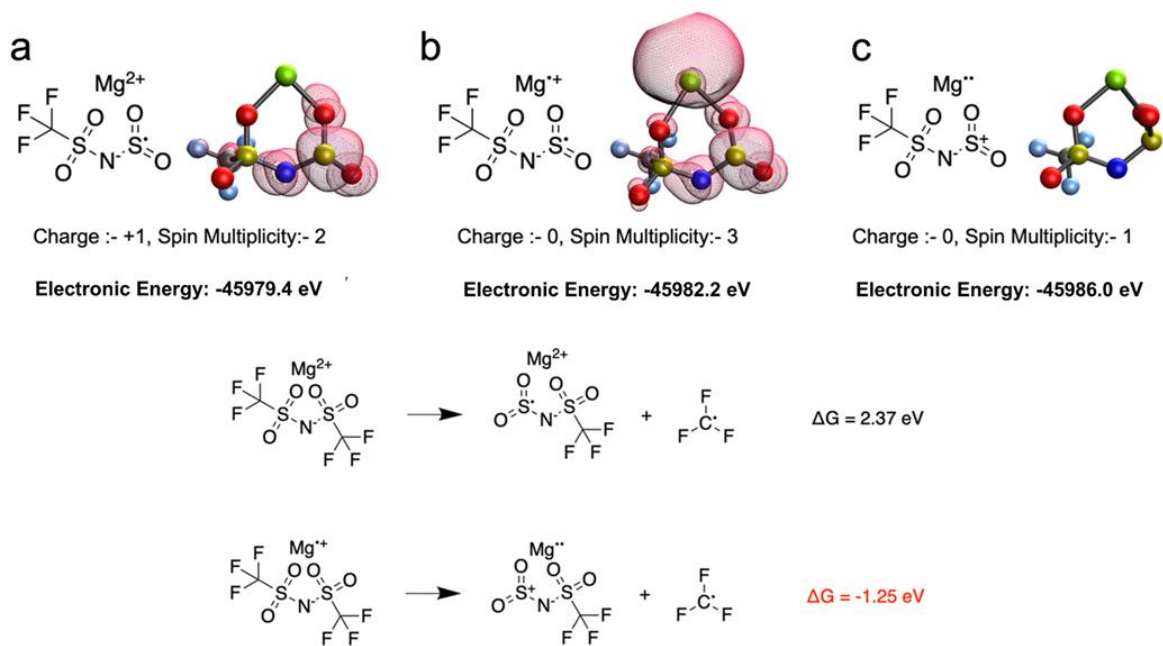
Fig. S7 Unpaired electron spin densities and electronic energies for potential products after dissociation of partially reduced CIP. (a) radical with 1 unpaired electron; (b) radical with 2 unpaired electrons; (c) radical with 0 unpaired electrons. The lowest energy radical (c) is assumed to be the dissociation product for the BDE calculations of the partially reduced CIP.
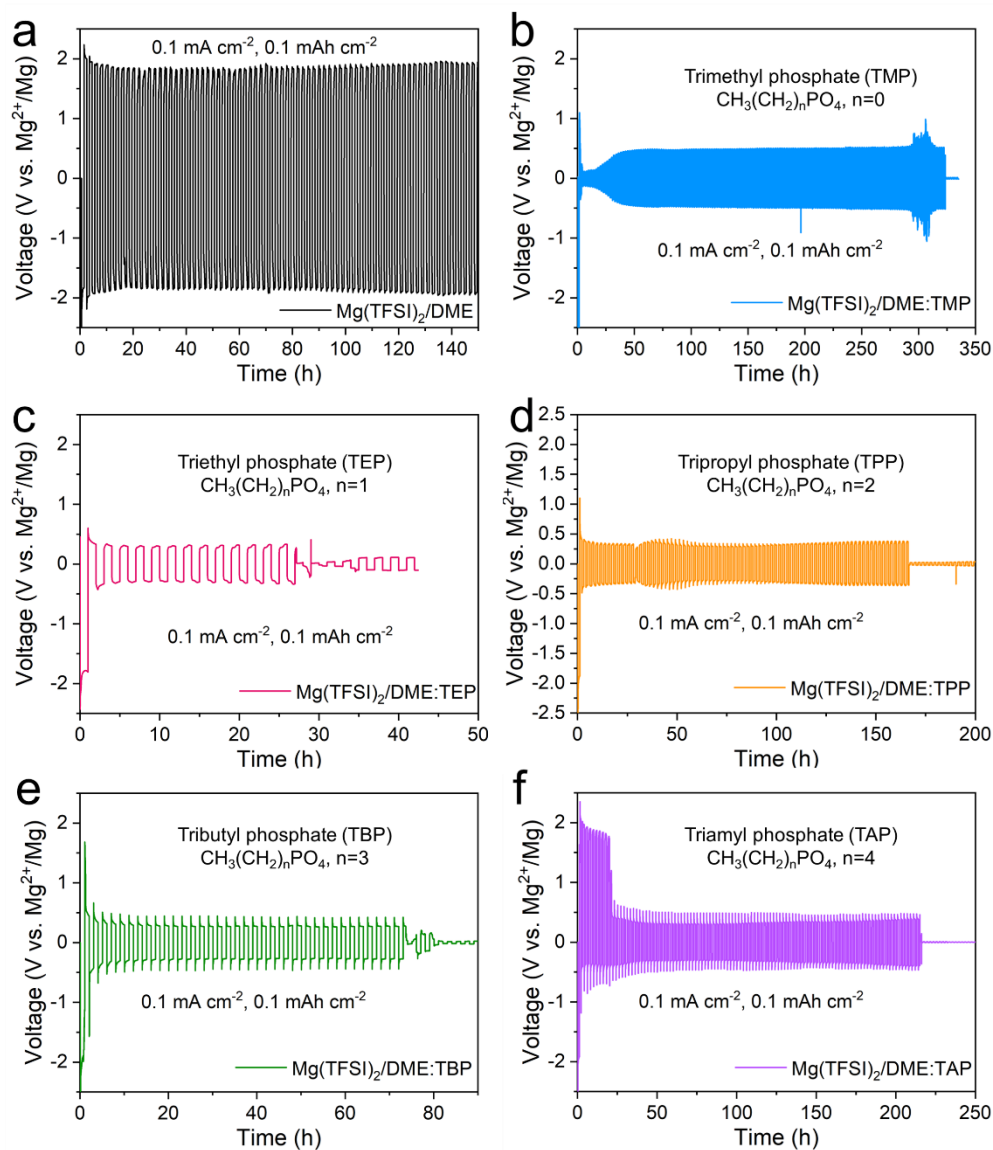
Fig. S8 Galvanostatic cycling of Mg symmetric cells with different phosphates. (a) Mg(TFSI)$_2$/DME; (b)Mg(TFSI)$_2$/DME:TMP; (c) Mg(TFSI)$_2$/DME:TEP; (d) Mg(TFSI)$_2$/DME:TPP; (e) Mg(TFSI)$_2$/DME:TBP; (f) Mg(TFSI)$_2$/DME:TAP. The current density is 0.1 mA cm^{-2} with an areal capacity of 0.1 mAh cm^{-2}. The DME: phosphate ratio is 10:1 in all cases.
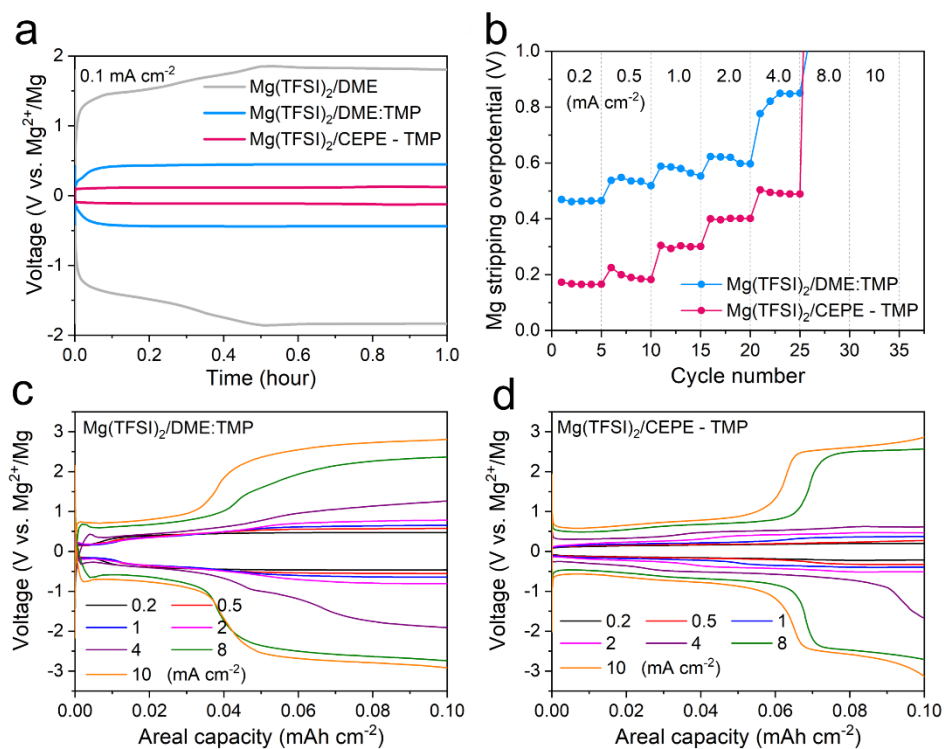
Fig. S9 Electrochemical performance of Mg plating/stripping in TMP-based electrolytes. (a) The 20th voltage profiles of Mg‖Mg symmetric cells with different electrolytes at a current density of 0.1 mA cm⁻² for 1 h. (b-d) Rate performance of Mg‖Mg symmetric cells and corresponding selected voltage profiles in c) Mg(TFSI)₂/DME:TMP and (d) Mg(TFSI)₂/CEPE-TMP. The areal capacity was fixed as 0.1 mAh cm⁻², and the stripping overpotential at the central point was collected.
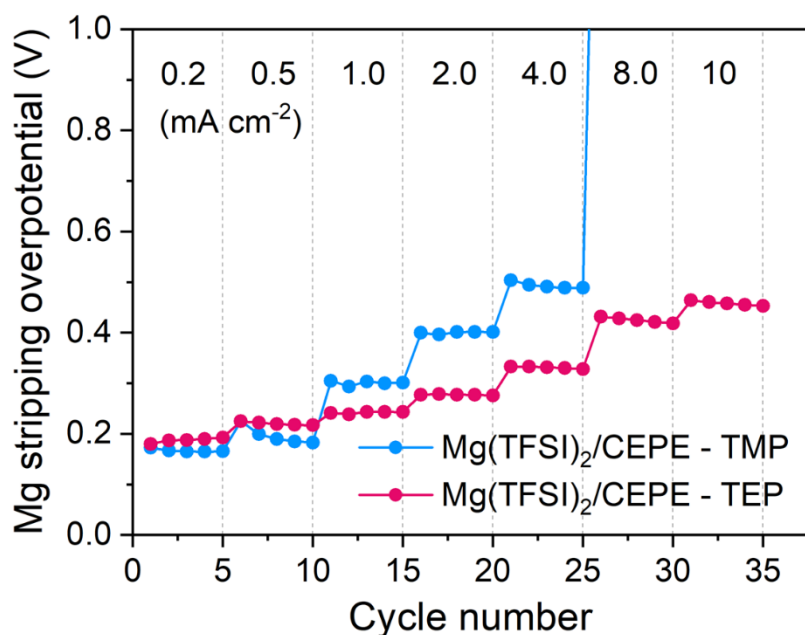
Fig. S10 Rate performance of Mg‖Mg symmetric cells in different CEPEs, where the phosphate is TMP or TEP.
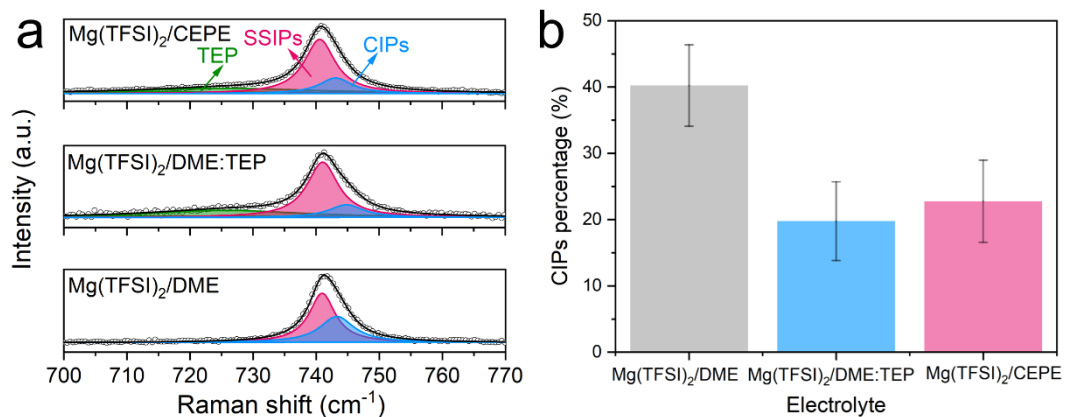
Fig. S11 Raman analysis of different electrolytes; (a) Fitted Raman spectra of different electrolytes in the region of 700-770 cm^{-1}. (b) CIP fraction in different electrolytes.
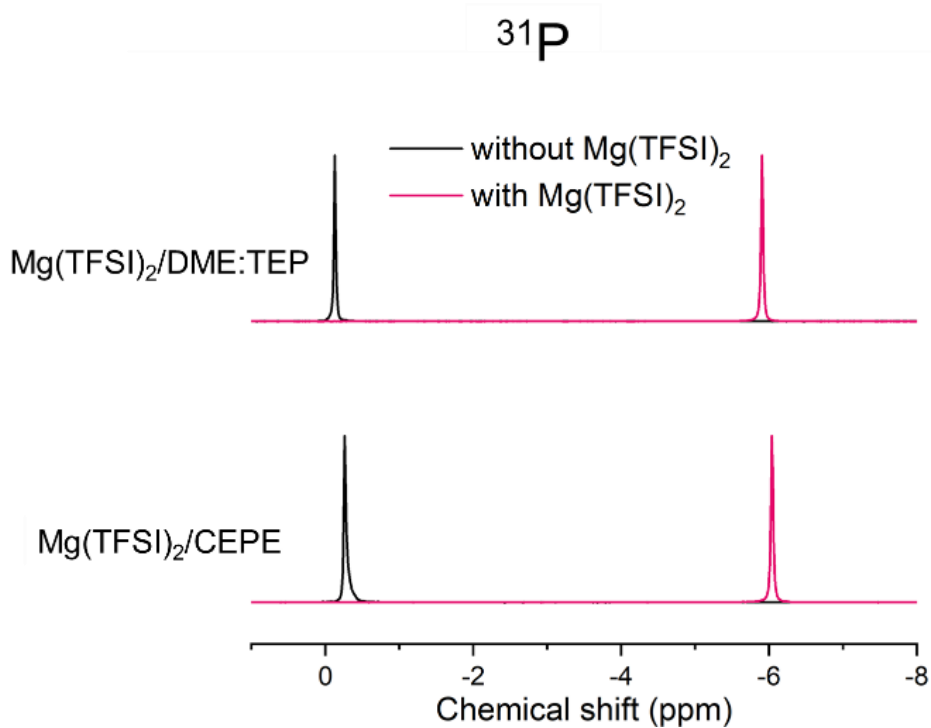
Fig. S12 ^{31}P NMR spectra of Mg(TFSI)$_2$/DME:TEP and Mg(TFSI)$_2$/CEPE at 298 K.
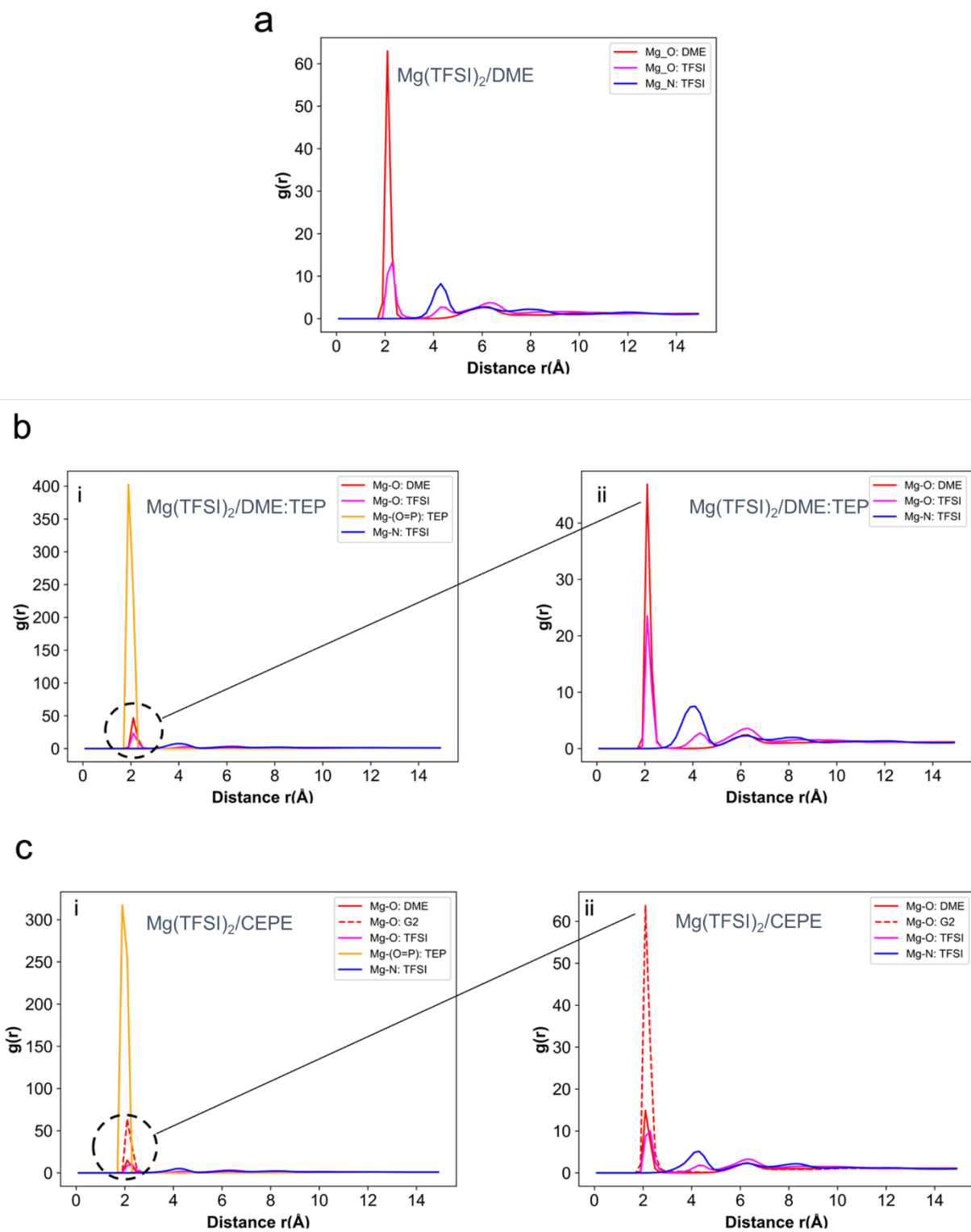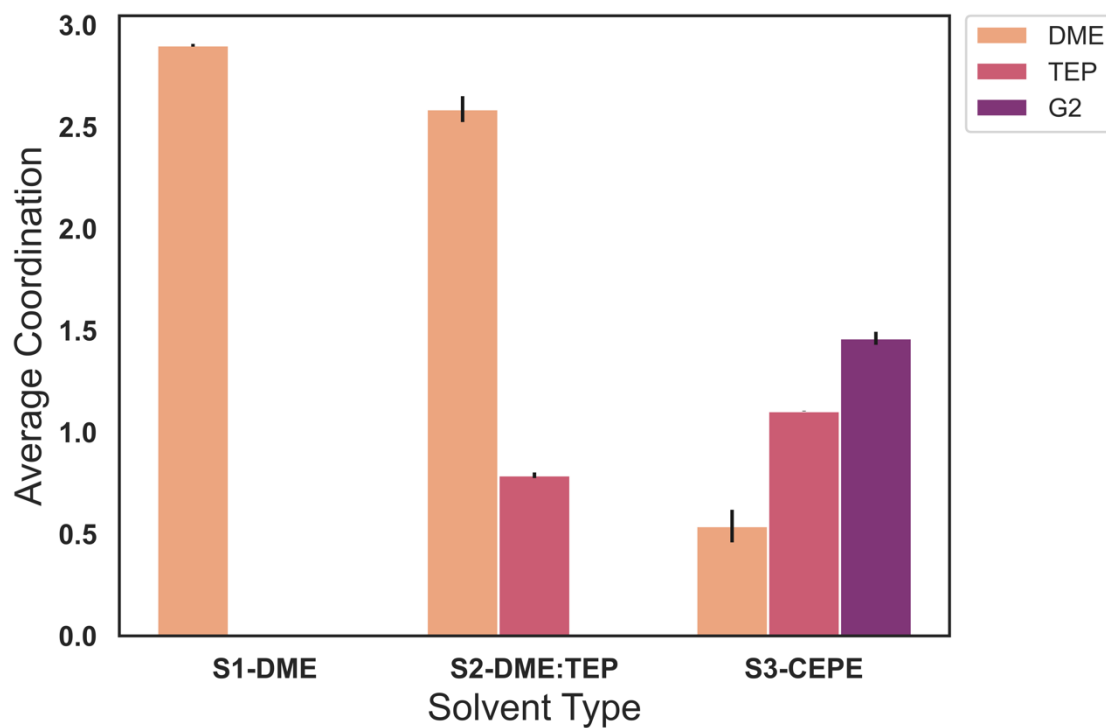
Fig. S13 Radial distribution functions of different coordinating species: in (a) Mg(TFSI)₂/DME system; (b) Mg(TFSI)₂/DME:TEP system; (c) Mg(TFSI)₂/CEPE system.
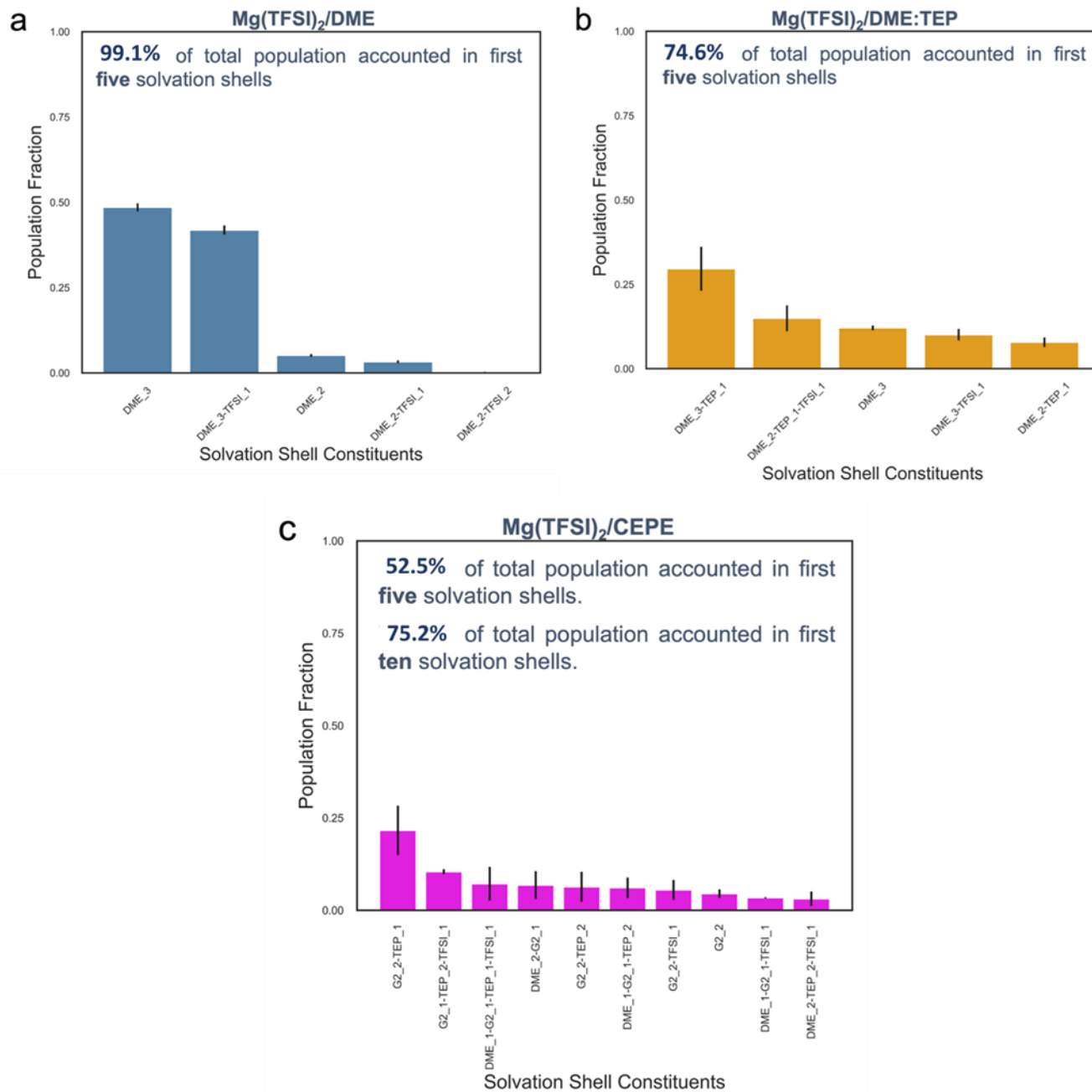
Fig. S14 Population fractions of different solvation shell species in the three electrolyte systems.
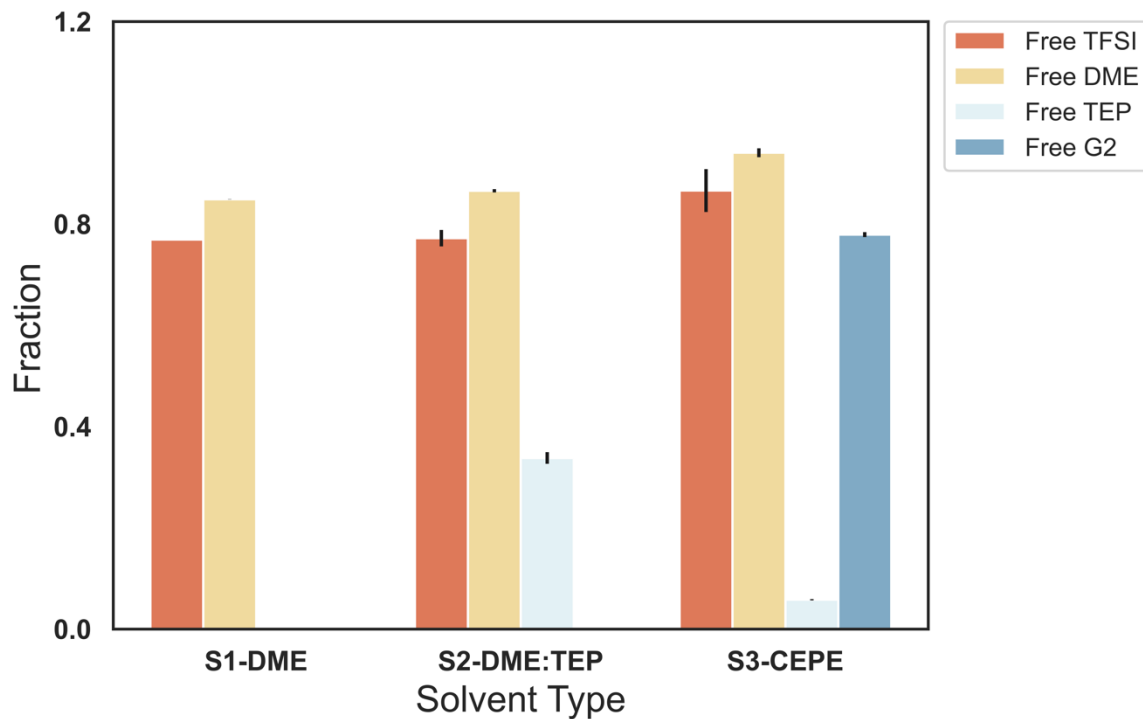
Fig. S15 Free solvent fractions of the different coordinating species in the three electrolyte systems.
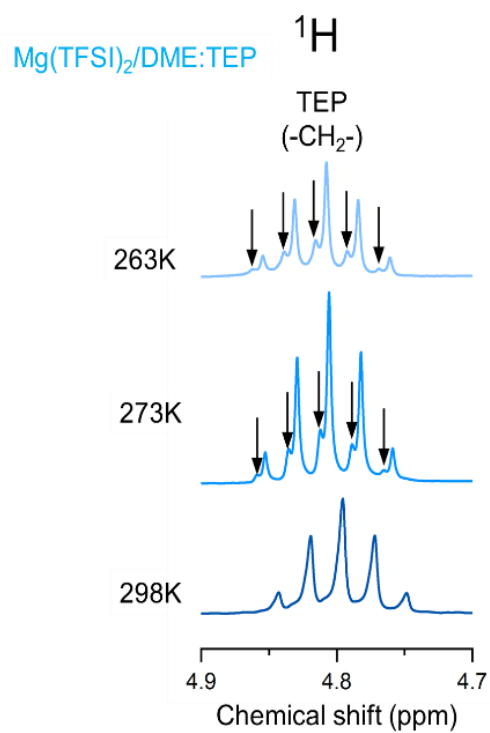

Fig. S16 Average coordination between Mg and the different solvent molecules in the three electrolyte systems.
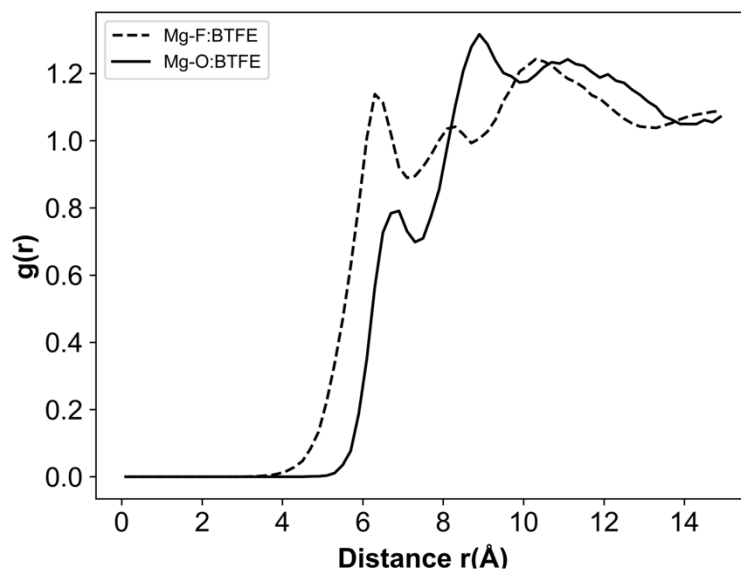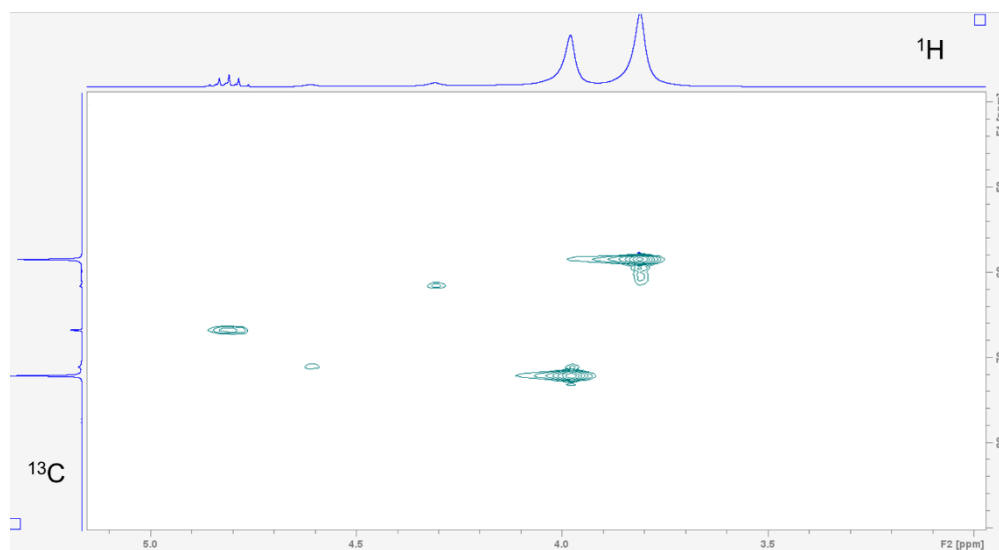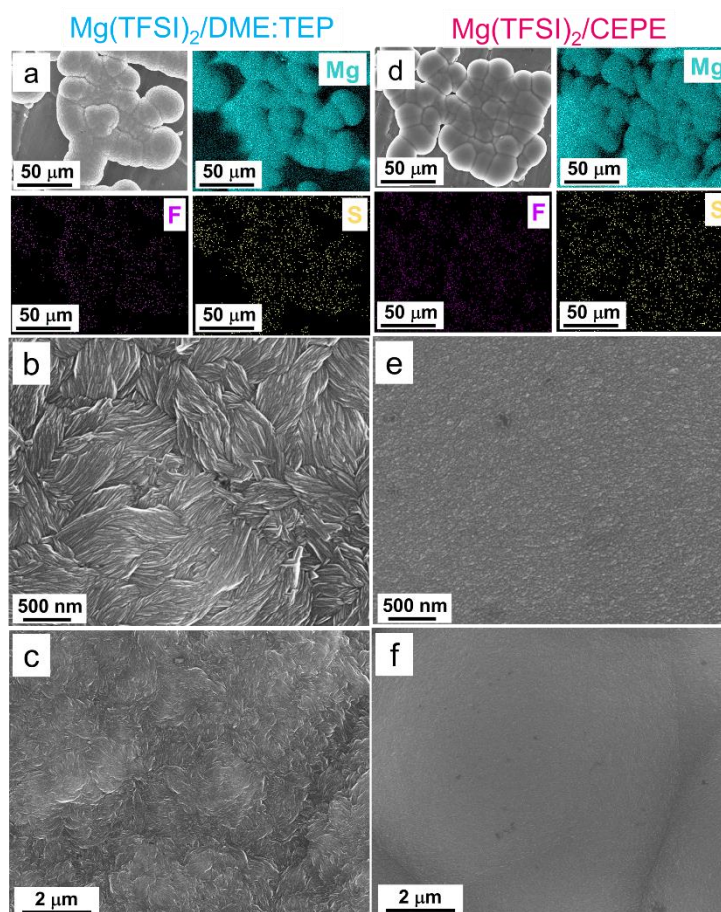
Fig. S17 Radial distribution functions for BTFE confirming the negligible Mg-BTFE interactions in the CEPE system.
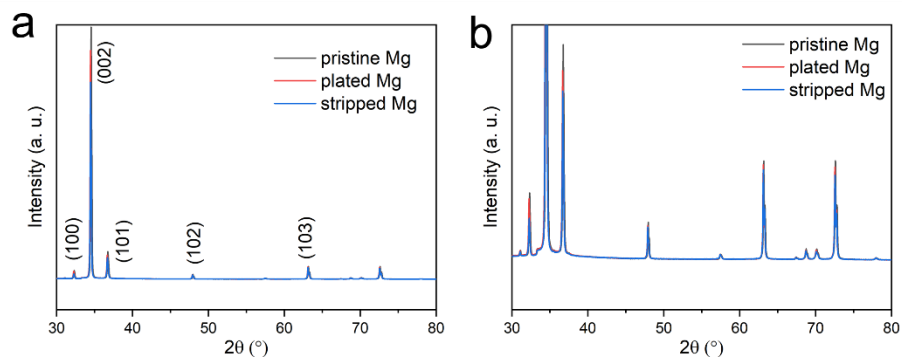

Fig. S18 Variable temperature ^{1}H NMR spectra of Mg(TFSI)$_2$/DME:TEP.

Fig. S19 HSQC plot of Mg(TFSI)$_2$/DME:TEP at 263 K with ^{1}H spectra at the top and ^{13}C spectra at the left.

**Fig. S20** SEM and EDX mapping images of plated Mg in TEP-based electrolytes: (a-c) Mg(TFSI)$_2$/DME:TEP; (d-f) Mg(TFSI)$_2$/CEPE.

Fig. S21 (a) XRD patterns of pristine, plated and stripped Mg anodes at 1 mA cm^{-2} (1 mAh cm^{-2}); (b) magnified view. Compared to the pristine Mg metal anode, plated and stripped Mg exhibit insignificant changes in XRD peak positions and intensities, indicating the plated Mg globules are agglomerated fine particles without preferred orientation or texture.
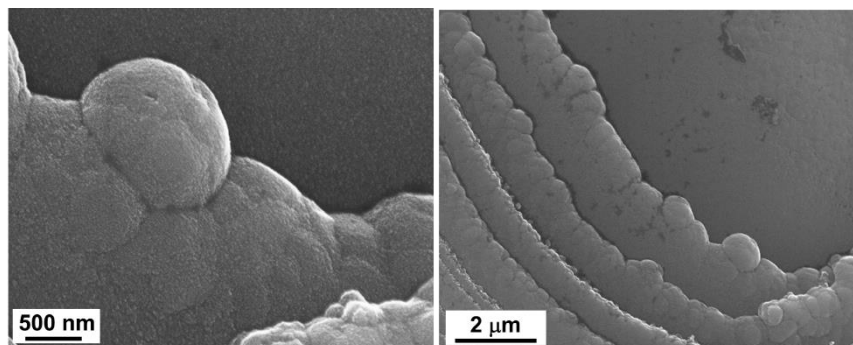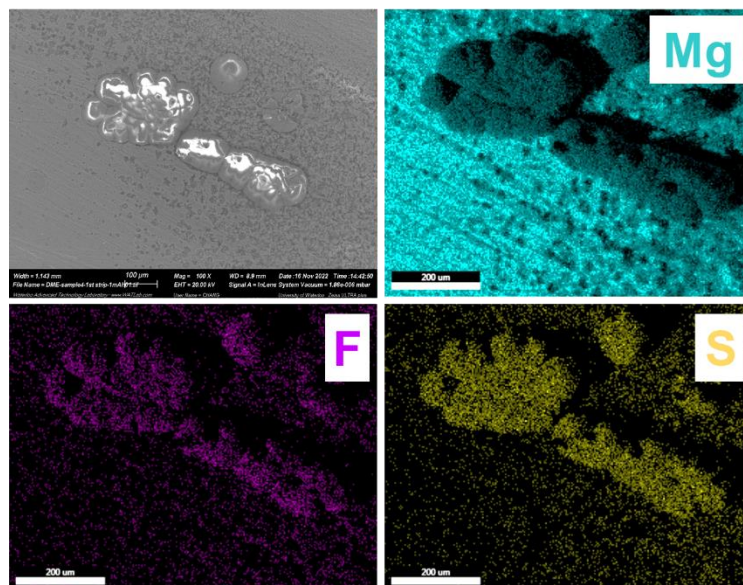

Fig. S22 SEM images of plated Mg in Mg(TFSI)$_2$/DME.

Mg(TFSI)₂/DME:TEP   Mg(TFSI)₂/CEPE
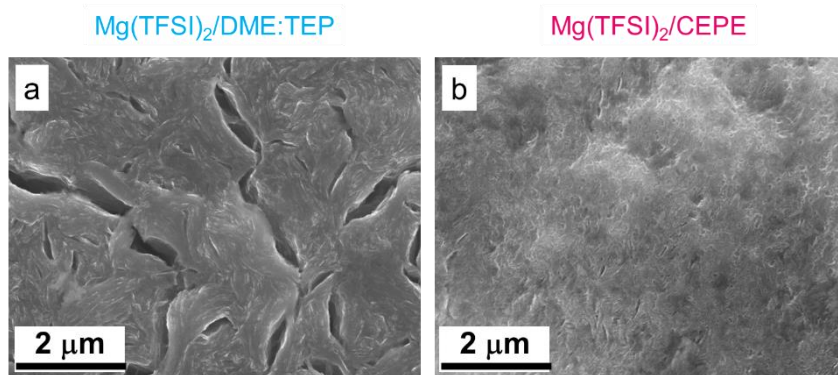
Fig. S23 SEM images of a half-stripped Mg electrode in TEP-based electrolytes: (a) Mg(TFSI)$_2$/DME:TEP; (b) Mg(TFSI)$_2$/CEPE.

Mg(TFSI)₂/DME:TEP   Mg(TFSI)₂/CEPE
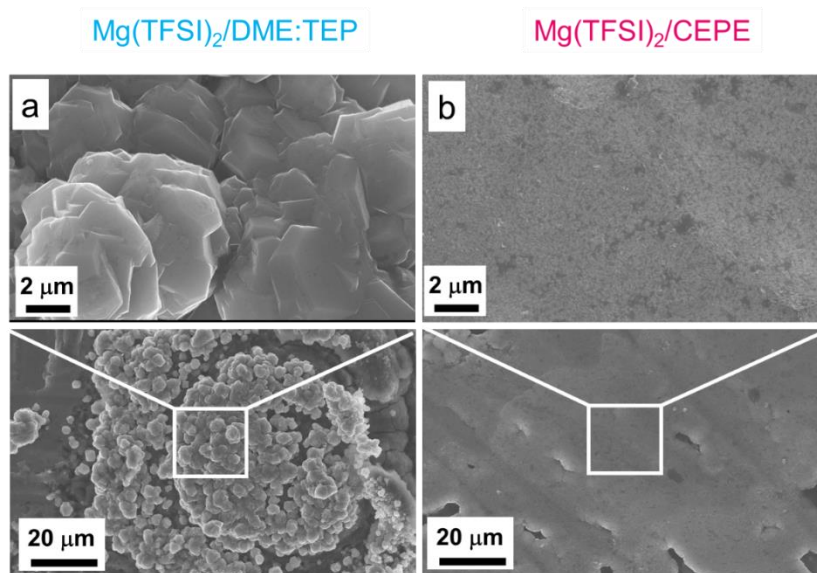

Fig. S24 SEM images of multiple-cycled Mg in TEP-based electrolytes: (a) Mg(TFSI)$_2$/DME:TEP after 10 cycles; (b) Mg(TFSI)$_2$/CEPE after 50 cycles.

Fig. S25 EDX map images of fully stripped Mg in Mg(TFSI)$_2$/DME.
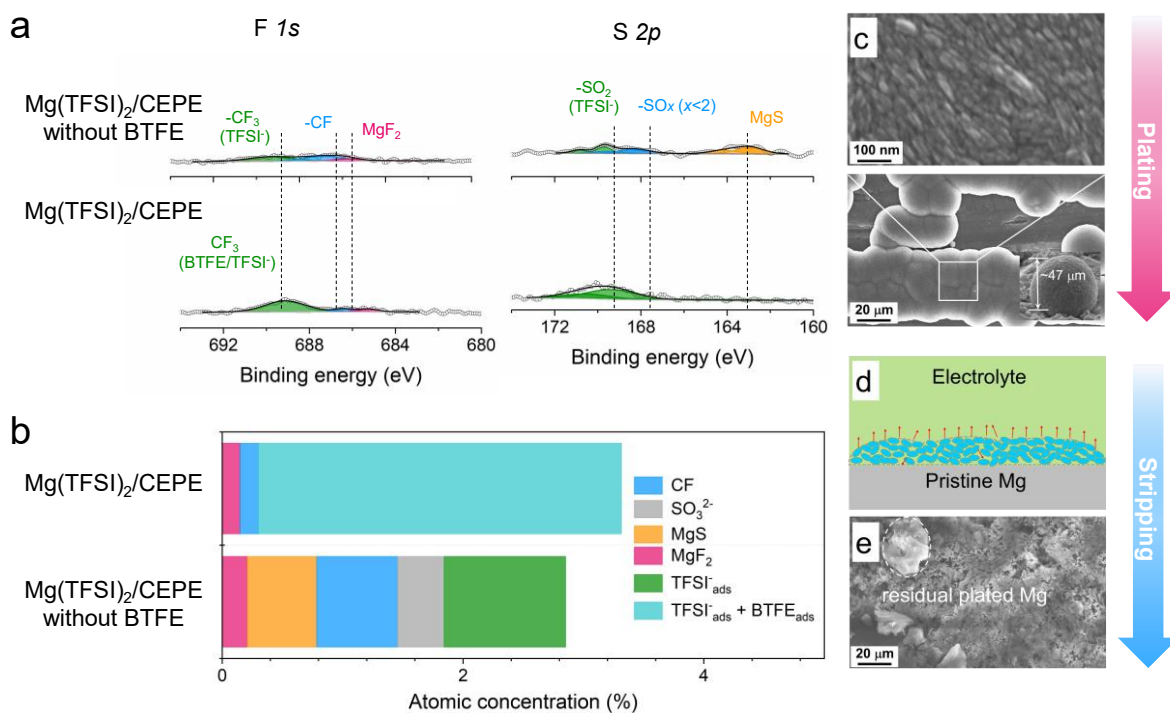
Fig. S26 XPS analysis of plated Mg in Mg(TFSI)$_2$/CEPE with/out BTFE. (a) F *1s* and S *2p* XPS spectra of plated Mg; (b) Atomic concentration of different TFSI$^-$-related species on the plated Mg surface. (c) Plated Mg morphology; (d) schematic illustration of stripping current distribution on plated Mg and (e) fully stripped morphology in Mg(TFSI)$_2$/CEPE without BTFE (0.4 M Mg(TFSI)$_2$/DME:G2:TEP [5:5:1 in vol]). Compared to the plating/stripping morphologies in Mg(TFSI)$_2$/CEPE (**Fig. 4**), in the absence of BTFE, significant larger Mg nuclei and residual plated Mg is observed on plated Mg globules and the fully stripped electrode, respectively. This confirms the benefit of trace BTFE to facilitate nanoscale Mg nucleation and growth.
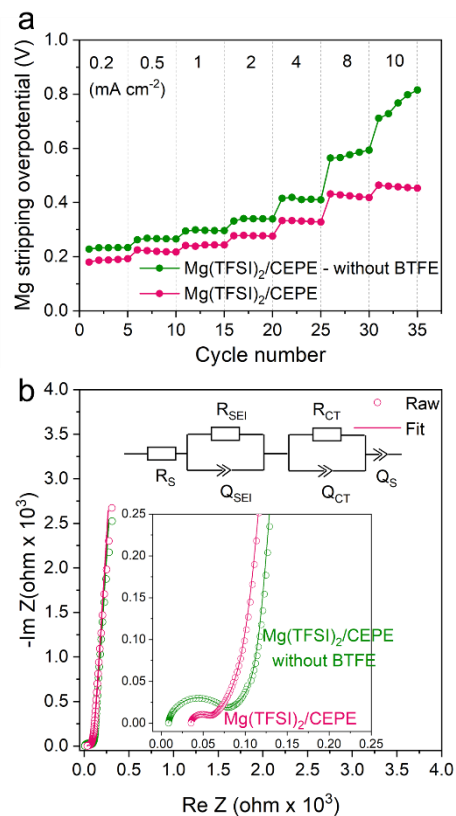
Fig. S27 Electrochemical performance of Mg plating/stripping in Mg(TFSI)$_2$/CEPE with/out BTFE. (a) Rate performance of Mg||Mg symmetric cells. The areal capacity was fixed as 0.1 mAh cm^{-2}, and the stripping overpotential at the central point was collected; (b) Nyquist plots of Mg||Mg symmetric cell after 10 cycles. The data were fit (shown by line) with the indicated equivalent circuit.
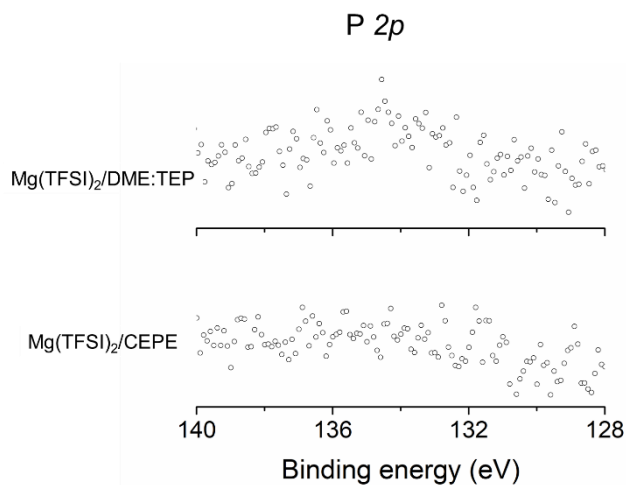
Fig. S28 XPS in the P $2p$ region of plated Mg in different electrolytes.
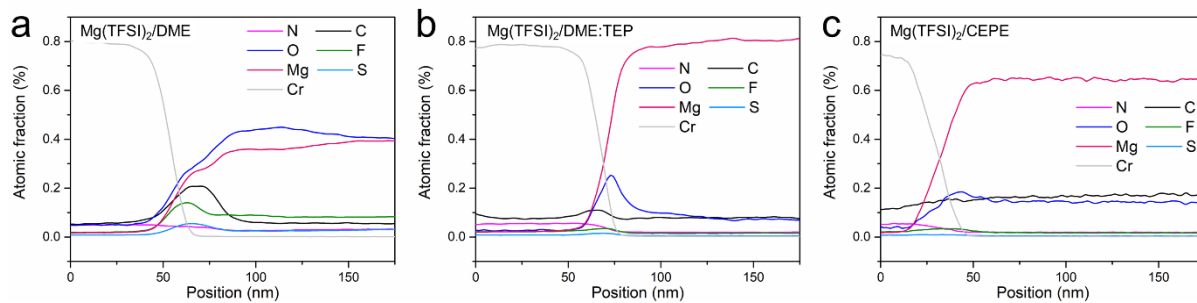
Fig. S29 The elemental distribution of an EDX line scan analysis taken along the indicated lines shown in the STEM-HADDF images in Fig. 7.
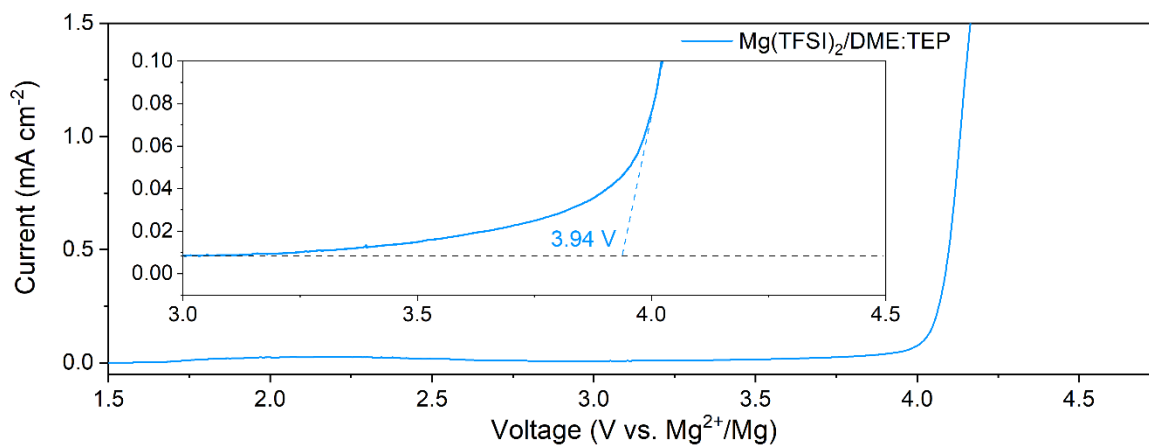
Fig. S30 LSV curve of Mg(TFSI)$_2$/DME:TEP at a scan rate of 5 mV s^{-1}.
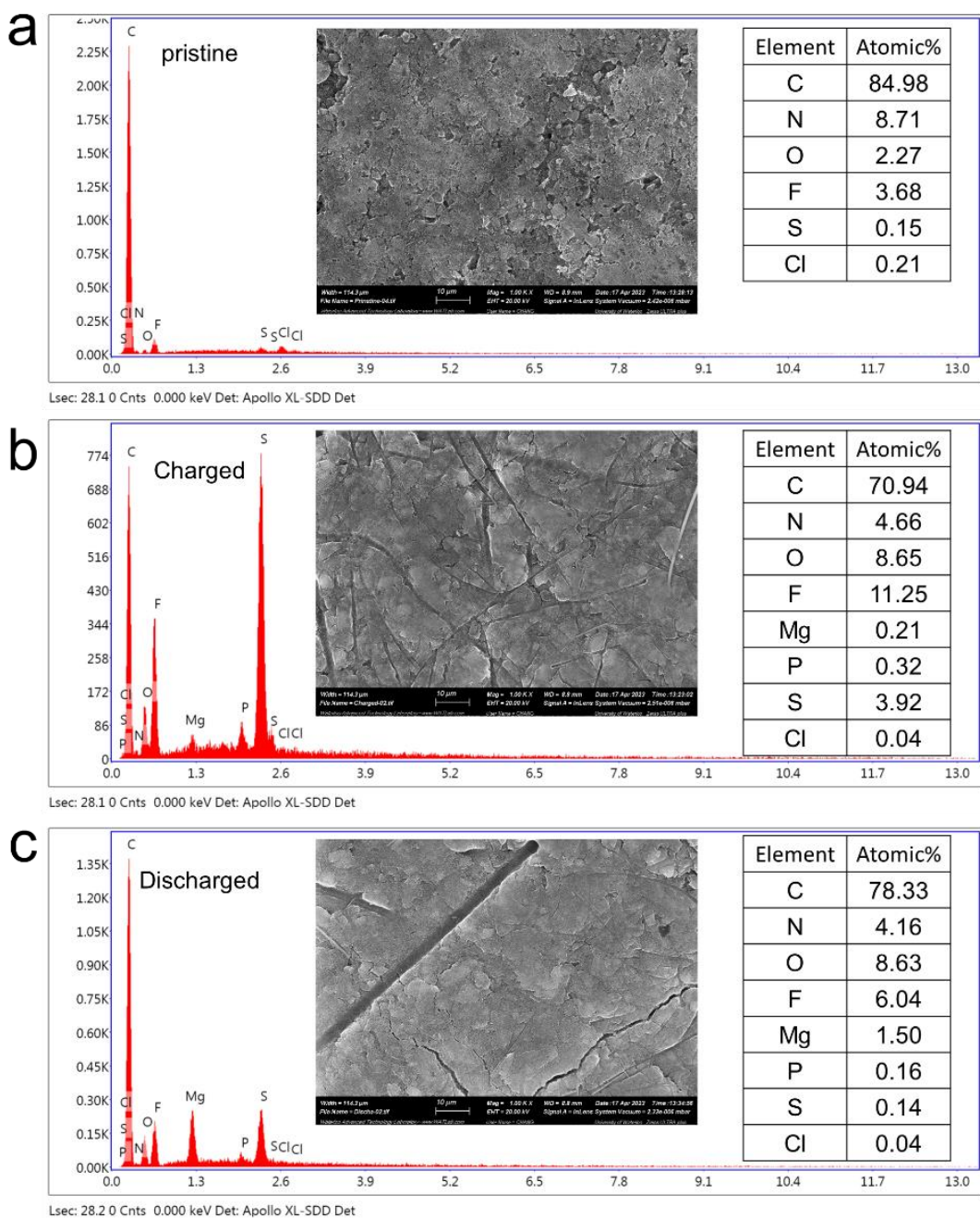
Fig. S31 SEM and EDX of (a) pristine, (b) charged and (c) discharged PANI in Mg(TFSI)$_2$/CEPE at C/10.
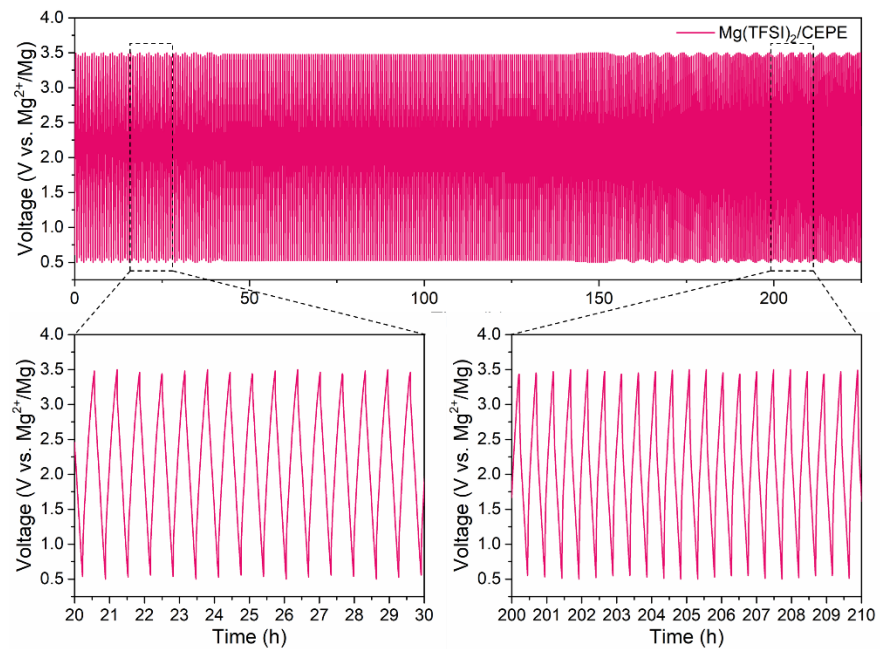
Fig. S32 Voltage profiles of PANI||Mg cells at a 2C rate in Mg(TFSI)$_2$/CEPE.
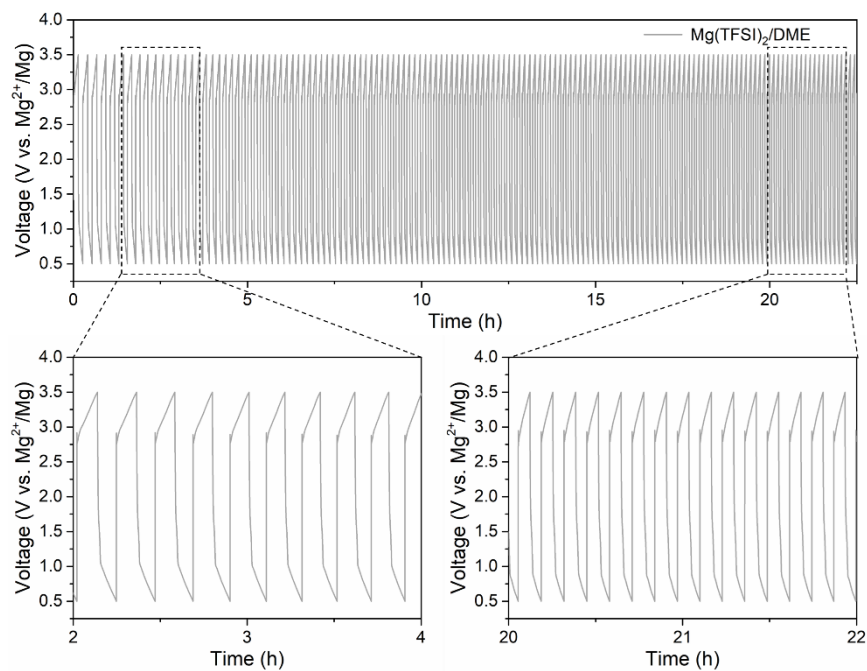
Fig. S33 Voltage profiles of PANI||Mg cells at a 2C rate in Mg(TFSI)$_2$/DME.
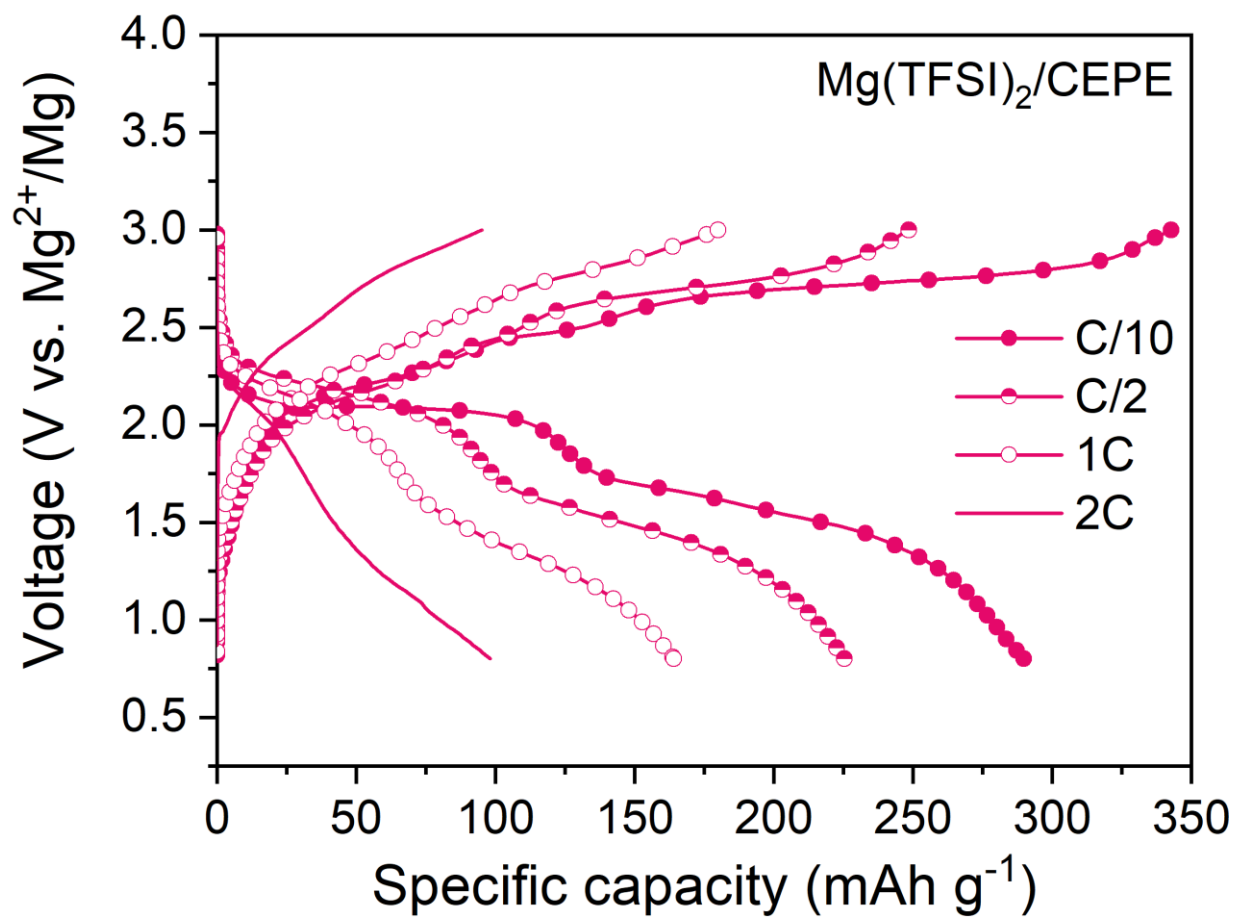
Fig. S34 Charge-discharge curve of PTO‖Mg cells at different rates (1C = 408 mA g_{PTO}^{-1}) in Mg(TFSI)$_2$/CEPE

Table S1 The compositions of different electrolytes. To prepare each electrolyte, 0.5 mmol Mg(TFSI)$_2$ was dissolved in 1 ml ethereal solvent with/out additional 0.1 ml TEP, to yield a total electrolyte volume of ~1.2 ml and a molarity of ~ 0.4 M.

Electrolytes (0.4 M Mg(TFSI)$_2$)	Solvents			
	DME (vol%)	G2 (vol%)	BTFE (vol%)	TEP (vol%)
Mg(TFSI)$_2$/DME	100	-	-	-
Mg(TFSI)$_2$/DME:TEP	100	-	-	10
Mg(TFSI)$_2$/CEPE	47.5	47.5	5	10

**Table S2** The comparison of ether-phosphate, chloride-based and organoborates-based Mg electrolytes. The reported performance of Mg||Mg symmetric cells are summarized based on current density, plating capacity per cycle and cycling stability (electrolytes with at least 500-hour cycle life were selected). CE of Mg plating/stripping was based on Mg||substrate asymmetric cells. Anodic stability is reported based on an aluminum substrate.

Electrolyte	Current density (mA cm^{-2})	Areal capacity per cycle (mAh cm^{-2})	Cycling stability (hours)	Cumulative capacity (mAh cm^{-2})	CE of Mg plating/ stripping	Anodic stability (V vs. Mg^{2+}/Mg)	Commercial availability
Mg(TFSI)$_2$/CEPE (this work)	2	2	7000	14000	95.2	4.2	Yes
Mg(TFSI)$_2$-MgCl$_2$ / DME:THF [23]	1	1	700	700	98.8	N/A	Yes
MgCl$_2$-AlCl$_3$- Mg(TFSI)$_2$ / DME [24]	0.025	0.0125	2000	50	96	1.1	Yes
MgCl$_2$-LiCl / THF [25]	0.05	0.2	700	35	97.5	N/A	Yes
Mg(OTf)$_2$-MgCl$_2$ / DME [26]	0.5	1	500	250	99.2	1.9	Yes
Mg[B(OCH(CF$_3$)$_2$)$_4$]$_2$ / DME [27]	0.1	0.1	1200	120	98%	~ 3.8	No
Mg[B(O$_2$C$_2$(CF$_3$)$_4$)$_2$]$_2$ / G2 [28]	0.1	N/A	500	50	95%	4.0	No
Mg(CB$_{11}$H$_{12}$)$_2$ /DME:G2 [2]	20	3	83.3	1666	99.9%	< 3.5	No

Table S3 The FWHM of the -CH$_2$ carbon peak of DME in ^{13}C spectra. Without Mg(TFSI)$_2$ salt, the addition of TEP to DME has no impact on the FWHM of DME. In contrast, in the presence of Mg(TFSI)$_2$, the FWHM of DME decreases by 60%. Since a large FWHM corresponds to cluster and CIP formation, this decrease indicates the Mg^{2+}-TEP interaction very effectively suppresses the formation of CIPs.

-CH$_2$ carbon of DME in ^{13}C spectra	FWHM (Hz)
DME	2.213
DME:TEP (10:1 in vol)	2.215
Mg(TFSI)$_2$/DME	18.441
Mg(TFSI)$_2$/DME:TEP	7.306

Table S4 Dielectric constants for the PCM dielectric calculations. The dielectric constant of DME and TEP were obtained from: https://www.stenutz.eu/chem/ and https://pubchem.ncbi.nlm.nih.gov/.

Electrolytes (0.4 M Mg(TFSI)$_2$)	Solvents								Effective Dielectric Constant
	DME		G2 (vol%)		BTFE (vol%)		TEP (vol%)		
	Dielectric Constant	Vol (%)	Dielectric Constant	Vol (%)	Dielectric Constant	Vol (%)	Dielectric Constant	Vol (%)	
Mg(TFSI)$_2$/DME	7.2	100	7.23[29]	-	4.4[30]	-	13.1	-	7.2
Mg(TFSI)$_2$/DME:TEP		100		-		-		10	8.51
Mg(TFSI)$_2$/CEPE		47.5		47.5		5		10	8.39

References

1. B. D. Adams, J. Zheng, X. Ren, W. Xu and J.-G. Zhang. *Adv. Energy Mater.*, 2018, **8**, 1702097.

2. H. Dong, O. Tutusaus, Y. Liang, Y. Zhang, Z. Lebens-Higgins, W. Yang, R. Mohtadi and Y. Yao. *Nat. Energy*, 2020, **5**, 1043–1050.

3. L. Martínez, R. Andrade, E. G. Birgin and J. M. Martínez. *J. Comput. Chem.*, 2009, **30**, 2157–2164.

4. E. L. Pollock and J. Glosli. *Comput. Phys. Commun.*, 1996, **95**, 93–110.

5. A. P. Thompson, H. M. Aktulga, R. Berger, D. S. Bolintineanu, W. M. Brown, P. S. Crozier, P. J. in 't Veld, A. Kohlmeyer, S. G. Moore, T. D. Nguyen, R. Shan, M. J. Stevens, J. Tranchida, C. Trott, S. J. Plimpton. *Comput. Phys. Commun.*, 2022, **271**, 108171.

6. J. Wang, R. M. Wolf, J. W. Caldwell, P. A., Kollman and D. A. Case. *J. Comput. Chem.*, 2004, **25**, 1157–1174.

7. J. Wang, W. Wang, P. A., Kollman and D. A. *J. Mol. Graph. Model.*, 2006, **25**, 247–260.

8. Z. Li, L. F. Song, P. Li and K. M. Merz. *J. Chem. Theory Comput.*, 2020, **16**, 4429–4442.

9. I. Leontyev and A. Stuchebrukhov. *Phys. Chem. Chem. Phys.*, 2011, **13**, 2613–2626.

10. B. J. Kirby and P. Jungwirth. *J. Phys. Chem. Lett.*, 2019, **10**, 7531–7536.

11. Z. Yu, T. R. Juran, X. Liu, K. S. Han, H. Wang, K. T. Mueller, L. Ma, K. Xu, T. Li, L. A. Curtiss, L. Cheng. *Energy Environ. Mater.*, 2022, **5**, 295–304.

12. O. A. Cohen, H. Macdermott-Opeskin, L. Lee, T. Hou, K. D. Fong, R. Kingsbury, J. Wang, and K. A. Persson. *J. Open Source Softw.*, 2023, **8**, 5183.

13. R. J. Gowers, M. Linke, J. Barnoud, T. J. E. Reddy, M. N. Melo, S. L. Seyler, J. Domanski, D. L. Dotson, S. Buchouxk, I. M. Kenney, O. Beckstein. *Proc. of the 15th Python in Science Conf.*, 2016, 98–105.

14. Epifanovsky, E. et al. *J. Chem. Phys.*, 2021, **155**, 084801.

15. E. W. C. Spotte-Smith, S. M. Blau, X. Xie, H. D. Patel, M. Wen, B. Wood, S. Dwaraknath and K. A. Persson. *Sci. Data*, 2021, **8**, 203.

16. K. Mathew, J. H. Montoya, A. Faghaninia, S. Dwarakanath, M. Aykol, H. Tang, I. Chu, T. Smidt, B. Bocklund, M. Horton, J. Dagdelen, B. Wood, Z. Liu, J. Neaton, S. P. Ong, K. A. Persson, A. Jain. *Comput. Mater. Sci.*, 2017, **139**, 140–152.

17. J.-D. Chai and M. Head-Gordon. *Phys. Chem. Chem. Phys.*, 2008, **10**, 6615.

18. D. Rappoport and F. Furche. *J. Chem. Phys.*, 2010, **133**, 134105.

19. J. Tomasi, B. Mennucci and R.Cammi. *Chem. Rev.*, 2005, **105**, 2999–3094.

20. N. Mardirossian and M. Head-Gordon. *J. Chem. Phys.*, 2016, **144**, 214110.

21. F. Weigend and R. Ahlrichs. *Phys. Chem. Chem. Phys.*, 2005, **7**, 3297–3305.

22. S. Grimme. *J. Comput. Chem.*, 2006, **27**, 1787–1799.

23. Y. Sun, Y. Wang, L. Jiang, D. Dong, W. Wang, J. Fan and Y. Lu. *Energy Environ. Sci.*, 2023, **16**, 265-274.

24. L. Yang, C. Yang, Y. Chen, Z. Pu, Z. Zhang, Y. Jie, X. Zheng, Y. Xiao, S. Jiao, Q. Li and D. Xu. *ACS Appl. Mater. Interfaces*, 2021, **13**, 26, 30712–30721.

25. Y. Han, G. Li, Z. Hu, F. Wang, J. Chu, L. Huang, T. Shi, H. Zhan, Z. Song. *Energy Storage Mater.*, 2022, **46**, 300-312.

26. D. Nguyen, A. Y. S. Eng, M. Ng, V. Kumar, Z. Sofer, A. D. Handoko, G. S. Subramanian, Z. W. She. *Cell Reports Physical Science*, 2020,**1**, 100265.

27. Z. Zhao-Karger, R. Liu, W. Dai, Z. Li, T. Diemant, B. P. Vinayan, C. B. Minella, X. Yu, A. Manthiram, R. J. Behm, M. Ruben and M. Fichtner. *ACS Energy Lett.*, 2018, **3**, 2005−2013.

28. J. Luo, Y. Bi, L. Zhang, X. Zhang and T. L. Liu. *Angew. Chem. Int. Ed.*, 2019, **58**, 6967–6971.

29. K. Hoshi, T. Chiba, J. Sato, Y. Hayashi, Y. Takahashi, H. Ebe, S. Ohisa and J. Kido. *ACS Appl. Mater. Interfaces*, 2018, **10**, 24607–24612.

30. W. W. A. van Ekeren, M. Albuquerque, G. Ek, R. Mogensen, W. R. Brant, L. T. Costa, D. Brandell and R. Younesi. *J. Mater. Chem. A*, 2023, **11**, 4111–4125.